

Transitions from Composite Fermi Liquid to Moore-Read States in Weyl Semimetals

Jiong-Hao Wang¹ and Yong Xu^{1,2*}

¹Center for Quantum Information, IIIS, Tsinghua University, Beijing 100084, People's Republic of China and

²Hefei National Laboratory, Hefei 230088, People's Republic of China

Weyl semimetals represent a significant class of topological gapless materials in three dimensions and have been shown to exhibit three-dimensional quantum Hall effect. However, existing research mainly focuses on scenarios without interactions. Recent studies suggest that the fractional quantum Hall effect can arise in a Weyl semimetal with a one-third filled Landau level under a magnetic field. However, it remains unclear whether more exotic states, such as composite Fermi liquid and Moore-Read states, can appear at half filling. Here we surprisingly find the existence of composite Fermi liquid, Moore-Read states and charge density waves in the same Weyl-orbit-based Landau level of a Weyl semimetal and their transitions induced by varying the distance between Weyl points. We attribute these transitions to a significant change in the single-particle wave functions of the Landau level as the distance between Weyl points is varied. Finally, we demonstrate that a transition from composite Fermi liquid to Moore-Read states can be induced by tuning the direction of a magnetic field, a process that is more experimentally accessible.

INTRODUCTION

Weyl semimetals [1–5], a prominent class of three-dimensional (3D) gapless topological materials, have attracted intense research interest in recent years [6–26]. Their band structures feature pairs of Weyl points that possess opposite topological charges and exhibit linear dispersion nearby. According to the bulk-boundary correspondence, the topology of the band structures leads to open Fermi surfaces (known as Fermi arcs) on the surface of a sample that connects projections of Weyl points with opposite charges. Due to the topological property, Weyl semimetals exhibit topological anomalous Hall effect [7, 8]. In addition, it has been shown that 3D quantum Hall effect can arise in Weyl semimetals or Dirac semimetals under a magnetic field [27–48] via Weyl orbits [12], a phenomenon that has recently been confirmed experimentally [31]. However, these studies mainly focus on scenarios without interactions.

It is well known that the interplay between topology and interactions can lead to exotic topological phases of matter in two dimensions (2D), such as fractional quantum Hall (FQH) states [49–53]. A typical example is the Laughlin FQH state at $1/m$ filling (m is an odd integer) that exhibits properties such as fractionally quantized Hall conductance as well as anyonic excitations with fractional charges and fractional statistics. Additionally, at various other filling factors with odd denominators, hierarchy FQH effect [53] can arise. They can be understood heuristically as an integer quantum Hall effect of composite fermions composed of bare electrons bound to an even number of vortices [54]. Beyond the odd denominator case, fascinating physics emerges at filling factors with even denominators. For example, at half filling of the lowest Landau level, there appears composite Fermi liquid (CFL) [55] where composite fermions feel zero effective magnetic fields. For the first excited Landau level, the Moore-Read (MR) state [56, 57] emerges,

which belongs to the non-Abelian FQH effect featuring non-Abelian anyons [56–58] with potential applications in topological quantum computation [58]. These phenomena have been extensively explored in 2D systems. Interestingly, recent developments have shown that Weyl semimetals can also exhibit FQH effect at one-third filling [48], based on the fact that Weyl semimetals can support Landau levels arising from Weyl orbits under a magnetic field. However, it remains an open question whether CFL and MR states can also appear in Weyl semimetals at half filling.

Here we theoretically study the ground state properties of electrons in Weyl semimetals under a magnetic field in the presence of Coulomb interactions, when a Landau level is half filled. We surprisingly observe a transition from the CFL to MR states and then to a charge density wave (CDW) in the same Landau level as we increase the separation between Weyl points. The transition is attributed to a significant change in the single-particle wave functions of the Landau level as the separation between Weyl points is varied. We identify the CFL phase by analyzing its low energy states in the many-body energy spectrum, which resemble those of the 2D CFL, and by examining the guiding center structure factor that reveals the Fermi surface of composite fermions. The MR states are identified through momentum-resolved low energy states in the energy spectrum and by counting eigenvalues below the gap in particle entanglement spectra, both of which are consistent with the (2,4) counting rule for MR states. As the separation between the Weyl points further increases, we observe a high degeneracy in the energy spectrum and prominent isolated peaks in the structure factor, indicating the presence of the CDW phase. Finally, we demonstrate that tuning the direction of a magnetic field can induce a transition from the CFL to MR states, a process that is more experimentally accessible.

MODEL

We start by considering a single-particle Weyl semimetal model described by the following continuous Hamiltonian [27, 48]

$$H(\mathbf{k}) = M[k_w^2 - (k_x^2 + k_y^2 + k_z^2)]\sigma_z + A(k_x\sigma_x + k_y\sigma_y) + [D_1k_y^2 + D_2(k_x^2 + k_z^2)]\sigma_0, \quad (1)$$

where σ_μ with $\mu = 0, x, y, z$ denote identity and Pauli matrices, respectively, $\mathbf{k} = (k_x, k_y, k_z)$ is the momentum, and M, A, D_1, D_2 , and k_w are system parameters. The model supports a pair of Weyl points at $(0, 0, \pm k_w)$. Under a magnetic field $\mathbf{B} = (0, B, 0)$ along y , the Weyl orbit formed by Fermi arcs [see Fig. 1(a)] gives rise to Landau levels. We here focus on the Landau level so that the total Chern number of all bands below this Landau level sums to zero (see Appendix A), and consider the case that this Landau level is half filled. We now investigate the possible phases in the half-filled Landau level with the Coulomb interaction between electrons in a sample geometry exhibiting a parallelogram shape with a $\theta = \pi/3$ inner angle in the horizontal plane [see Fig. 1(a)]. The interaction under periodic boundary conditions (PBCs) along \mathbf{e}_1 and \mathbf{e}_2 and open boundary conditions (OBCs) along y reads

$$V(\mathbf{r}) = \sum_{t,s=-\infty}^{+\infty} \frac{e^2}{4\pi\epsilon} \frac{1}{|\mathbf{r} + tL_1\mathbf{e}_1 + sL_2\mathbf{e}_2|}, \quad (2)$$

where e is the electron charge, ϵ is the dielectric constant, and \mathbf{e}_1 and \mathbf{e}_2 are unit vectors as shown in Fig. 1(a) with L_1 and L_2 being the system's length along these directions, respectively. Following the conventional single-band projection approximation in the study of Landau level physics [48, 59–62], which is the only approximation in our numerical calculations, we project the interactions onto the Landau level of interest and arrive at the interacting Hamiltonian

$$\hat{H}_I = \sum_{\mathbf{k}_1, \mathbf{k}_2, \mathbf{k}_3, \mathbf{k}_4} C_{\mathbf{k}_1 \mathbf{k}_2 \mathbf{k}_3 \mathbf{k}_4} \hat{c}_{\mathbf{k}_1}^\dagger \hat{c}_{\mathbf{k}_2}^\dagger \hat{c}_{\mathbf{k}_3} \hat{c}_{\mathbf{k}_4}. \quad (3)$$

Here $\hat{c}_{\mathbf{k}}$ ($\hat{c}_{\mathbf{k}}^\dagger$) is the annihilation (creation) operator of a single-particle state at a two-dimensional (2D) momentum $\mathbf{k} = k_1\mathbf{g}_1 + k_2\mathbf{g}_2$ in the considered Landau level, where $k_i = 0, 1, \dots, N_i - 1$ for $i = 1, 2$ with $N_1 N_2$ equal to the degeneracy of the Landau level, and $N_j \mathbf{g}_j$ ($j = 1, 2$) play the roles of reciprocal primitive vectors such that $\mathbf{g}_i \cdot \mathbf{e}_j = \delta_{ij} 2\pi/L_i$ (see Appendix B). In numerical calculations, we drop the quadratic terms that contribute a constant value [48], and focus solely on the pure interacting Hamiltonian (3). For simplicity, we consider the geometry with $N_1/N_2 = L_1/L_2$ so that the Brillouin zone is a hexagon (see Appendix B). We consider $N_1 = N_2 = 4$ for eight electrons, $N_1 = 4, N_2 = 5$ for ten electrons, and $N_1 = 4, N_2 = 6$ for twelve electrons.

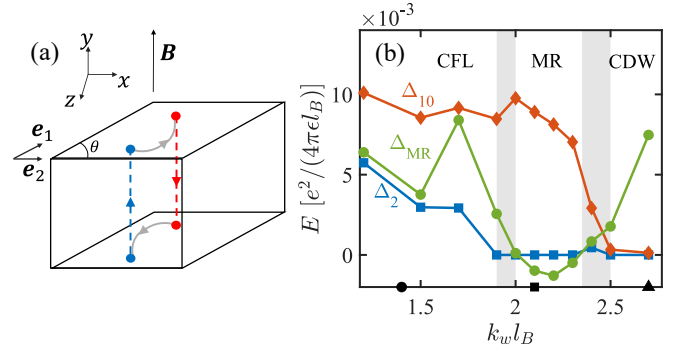


FIG. 1. (a) Schematic illustration of Fermi arcs (gray curves) and Weyl orbits developed under a magnetic field \mathbf{B} for the Hamiltonian (1) (see Appendix A). We consider a geometry characterized by a parallelogram in the horizontal plane, defined by two unit vectors \mathbf{e}_1 and \mathbf{e}_2 with an angle θ . (b) The phase diagram for the interacting Hamiltonian (3) at half filling with respect to half the distance between two Weyl points (k_w). Three phases including the CFL, the MR state and the CDW are identified. The energy differences Δ_2 (blue line), Δ_{10} (red line) and Δ_{MR} (green line) are defined in the main text. The critical regions are indicated by the gray color. The black circle, square and triangle on the k_w axis denotes the points with $k_w l_B = 1.4, 2.1, 2.7$, respectively. Here, $l_B = \sqrt{\hbar/(eB)}$ is the magnetic length. The Landau levels are calculated for the parameters $\tilde{M} = M/l_B^2 = 0.03E_0$, $\tilde{D}_1 = D_1/l_B^2 = 0.025E_0$, $\tilde{D}_2 = D_2/l_B^2 = 0.005E_0$ and $\tilde{A} = A/l_B = 0.04E_0$, with E_0 being the unit of energy. This set of parameters is used throughout the paper unless stated otherwise.

PHASE DIAGRAM

We find three strongly-correlated phases: CFL, MR states and CDW, as shown in Fig. 1(b). We see that the CFL first transitions to the MR states and then to the CDW as the distance between the two Weyl points increases. The three distinct phases are initially identified by calculating energy differences for a system with twelve electrons. A detailed analysis of these phases will be presented in the following sections. Specifically, since one of the ground states in the MR phase and CDW phase lie in the momentum sector with $k_1 + N_1 k_2 = 2$ [see Fig. 3(c)] and $k_1 + N_1 k_2 = 10$ [see Fig. 4(c)], respectively, the energy difference Δ_2 (Δ_{10}) between the lowest energy in the former (latter) momentum sector and the ground state energy of the system is able to reveal the transition from the CFL (MR state) to the MR state (CDW). Indeed, we see that as k_w increases, Δ_2 drops to zero near $k_w = 1.9$, indicating the transition to the MR state. Note that the ground states for the CFL phase do not appear in these momentum sectors [see Fig. 2(c)]. The sharp decline of the red line near $k_w = 2.4$ implies a transition to the CDW phase. In addition, we plot Δ_{MR} defined as the highest energy of the MR manifold minus the lowest energy of the other states ($-\Delta_{\text{MR}}$ indicates the energy gap

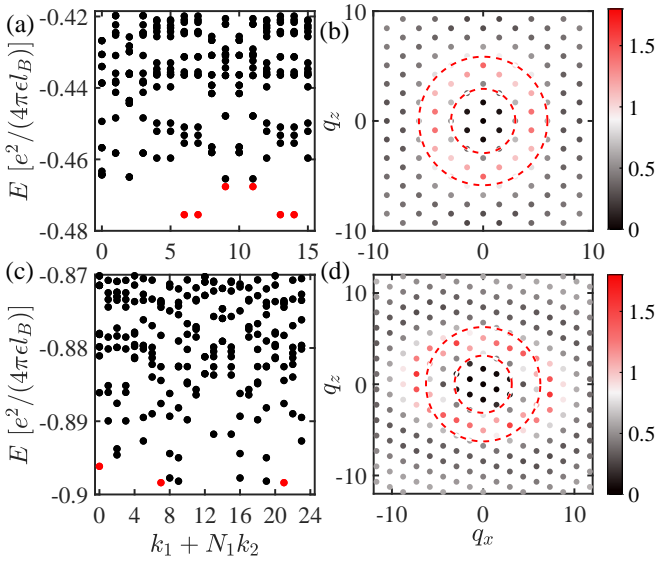


FIG. 2. The many-body energy spectrum for (a) eight and (c) twelve electrons at $k_w = 1.4/l_B$. The low energy states similar to the 2D CFL are colored red with each red point representing two degenerate states. The guiding center static structure factor $S(\mathbf{q})$ of the ground states for (b) eight and (d) twelve electrons. The inner red circle describes the Fermi surface of free electrons with the radius k_F and the outer one indicates $2k_F$.

in the MR phase). Here the MR manifold is composed of two lowest energy states with $k_1 + N_1 k_2 = 0$ and four lowest energy states with $k_1 + N_1 k_2 = 2$, which are just the MR states in the MR phase [see Fig. 3(c)]. When $\Delta_{\text{MR}} < 0$, it signifies a finite gap above the MR manifold, corresponding to the MR region with $\Delta_2 = 0$ and $\Delta_{10} > 0$ in Fig. 1(b).

In Appendix C, we show in detail that the phase transition arises due to the dramatic change in the single-particle wave functions of the considered Landau level as k_w increases. In the following, we will investigate the properties of the three phases in detail.

COMPOSITE FERMI LIQUID

We numerically diagonalize the Hamiltonian (3) exactly to obtain the many-body energy spectrum resolved by the total momentum at $k_w = 1.4/l_B$, as shown in Fig. 2(a) and (c) for eight and twelve electrons, respectively. We see that the low energy spectrum is similar to that of half-filled lowest Landau level in two dimensions, the paradigmatic CFL [63, 64] (see Appendix D), suggesting that the phase we find in Weyl semimetals is also the CFL. Explicitly, in Fig. 2(a), the twelve states with lowest energy (highlighted by the red color and each red point represents doubly degenerate states) appear in the same momentum sectors as the 2D CFL, which

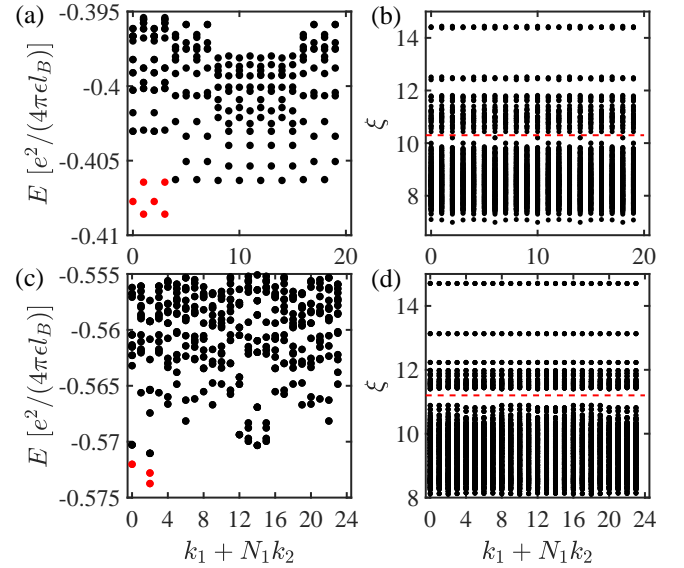


FIG. 3. The many-body energy spectrum for (a) ten and (c) twelve electrons when $k_w = 2.1/l_B$. The MR states are indicated by the red color. The particle entanglement spectrum for (b) ten and (d) twelve electrons. The number of states below the red dashed line is consistent with the counting rule for the MR states.

can be explained by the picture of stacking composite fermions [63, 65]. For $n_e = 12$ (n_e denotes the number of electrons) in Fig. 2(c), we mark the states with lowest energy (each is two-fold degenerate) in the momentum sectors where the ground states of the 2D CFL lie by the red color. We see that in two of them the states colored red are ground states of the system. In another one, the energy of the states colored red is a little higher than a few states in other momentum sectors, which is possible in a finite-size system considering the gapless nature of the CFL.

To provide further evidence showing that the system is in the CFL phase, we calculate the guiding center static structure factor [60, 62, 66] (also see Appendix E)

$$S(\mathbf{q}) = \frac{\langle \bar{\rho}(\mathbf{q})\bar{\rho}(-\mathbf{q}) \rangle}{n_e} - \frac{\langle \bar{\rho}(0) \rangle^2}{n_e}, \quad (4)$$

where $\bar{\rho}(\mathbf{q}) = \sum_i e^{i\mathbf{q} \cdot \mathbf{R}_i}$ with \mathbf{R}_i being the guiding center coordinate operator of the i th electron, $\mathbf{q} = q_1 \mathbf{g}_1 + q_2 \mathbf{g}_2$ with q_1, q_2 taking integer values, and $\langle \dots \rangle$ indicates the expectation value for the ground state. We plot the $S(\mathbf{q})$ in Fig. 2(b) and (d) for $n_e = 8$ and 12, respectively, and indicate the magnitude of the Fermi wave vector of free electrons k_F from the origin by an inner dashed red line and $2k_F$ by an outer dashed line. We see that $S(\mathbf{q})$ exhibits strong peaks on a closed loop near $|\mathbf{q}| = 2k_F$, indicating the Fermi surface of composite fermions [66, 67]. Note that the composite fermion Fermi surface for $n_e = 12$ is deformed from an exact circle, which may be attributed to the anisotropy of the Weyl semimetal

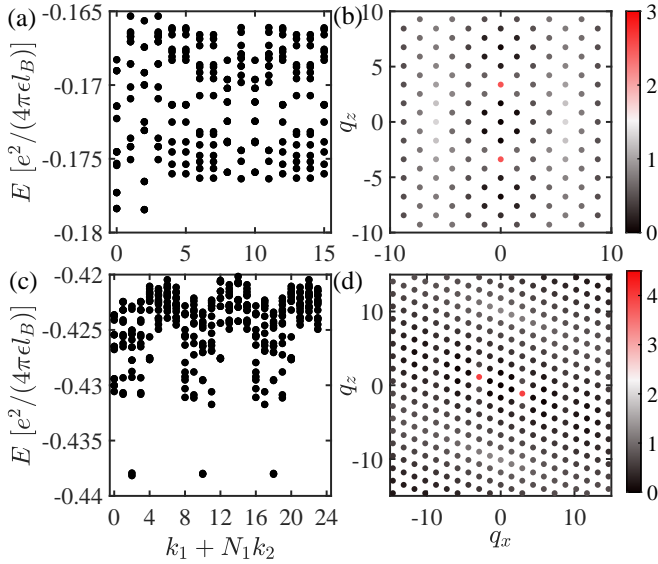


FIG. 4. The many-body energy spectrum for (a) eight and (c) twelve electrons when $k_w = 2.7/l_B$. The guiding center static structure factor $S(\mathbf{q})$ of the ground states for (b) eight and (d) twelve electrons.

Hamiltonian (1).

MOORE-READ STATES

We show the energy spectrum of the Hamiltonian (3) at $k_w = 2.1/l_B$ in Fig. 3(a) for ten electrons and (c) for twelve electrons. In both cases, we see six states with lowest energy (highlighted by red color and states in Fig. 3(c) are two-fold degenerate) lying in the exact momentum sector predicted by the (2, 4) counting rule of MR states [68], i.e. there are at most two electrons in four consecutive orbitals. To probe the excitation properties of the possible MR states, we calculate the particle entanglement spectrum [48, 69], i.e. the eigenvalues of the reduced density matrix

$$\rho_A = \text{Tr}_B \left(\frac{1}{6} \sum_{i=1}^6 |\Psi_i\rangle\langle\Psi_i| \right), \quad (5)$$

where the summation is over the six states with lowest energy. The reduced density matrix is obtained by tracing out n_b electrons in the B part out of the total n_e electrons with $n_a = n_e - n_b$ electrons left. The particle entanglement spectrum for $n_e = 10$ and $n_a = 4$ is shown in Fig. 3(b). We see a gap (indicated by the red dashed line) below which the numbers of eigenvalues in each momentum sector are 200, 196, 201, 196, 200, 196, 201, 196, ..., consistent with the (2, 4) counting rule of the MR states. A clearer gap manifests in Fig. 3(d) for $n_e = 12$ and $n_a = 4$ below which the numbers of eigenvalues are 394 for momentum sectors with $\text{mod}(k_1 + N_1 k_2, 8) = 0$,

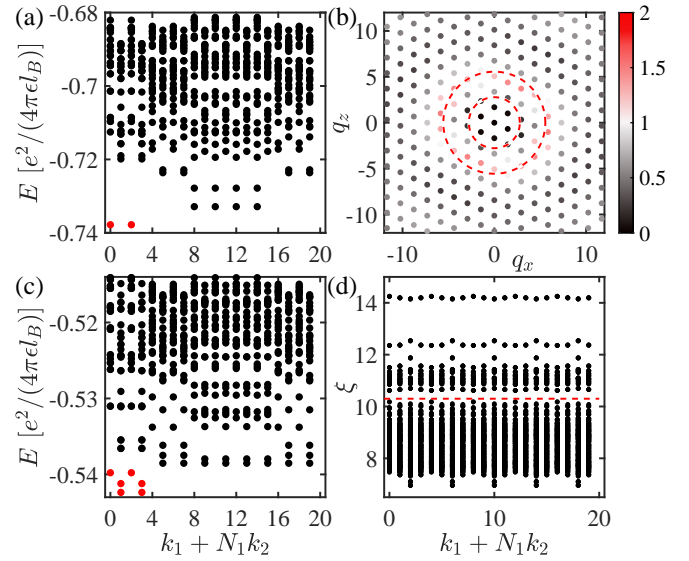


FIG. 5. (a) The many-body energy spectrum and (b) the guiding center static structure factor $S(\mathbf{q})$ of the ground state for ten electrons under vertical magnetic fields. In (a), the low energy states colored red are similar to these of the 2D CFL. (c) The many-body energy spectrum and (d) the particle entanglement spectrum for ten electrons under a tilted magnetic field. The number of states below the red dashed line agrees with the counting rule of the MR states. Here, we take $\tilde{M} = M/l_B^2 = 0.05E_0$, $\tilde{D}_1 = D_1/l_B^2 = 0.025E_0$, $\tilde{D}_2 = D_2/l_B^2 = 0.005E_0$, $\tilde{A} = A/l_B = 0.05E_0$, and $k_w = 1.7/l_B$.

396 for $\text{mod}(k_1 + N_1 k_2, 8) = 2$ and 384 for others, also satisfying the counting rule of MR states. Thus, the particle entanglement spectrum provides further evidence that the states are indeed the MR states. Interestingly, for the half-filled first excited Landau level in 2D with Coulomb interactions, commonly regarded as the MR states, a gap below which the number of states satisfies the MR counting rule exists when $n_e = 10$ and $n_a = 4$ but is absent when $n_e = 12$ and $n_a = 4$ [70].

CHARGE DENSITY WAVES

We now provide evidence showing that the ground states are CDWs when $k_w = 2.7/l_B$. Figure 4(a) displays the many-body energy spectrum for eight electrons, illustrating quasi-degenerate ground states in momentum sectors with $k_1 + N_1 k_2 = 0$ and 2, each having four-fold degeneracy. For twelve electrons as shown in Fig. 4(c), we see twelve quasi-degenerate ground states in $k_1 + N_1 k_2 = 2, 10, 18$ momentum sectors with four-fold degeneracy in each momentum sector. The high degeneracy seen here is often a signature of CDWs [60, 61]. To elucidate the properties of the states, we calculate $S(\mathbf{q})$ and show them in Fig. 4(b) and (d) for eight and twelve electrons, respectively. The figures exhibit two isolated sharp peaks, obviously evidencing a CDW phase.

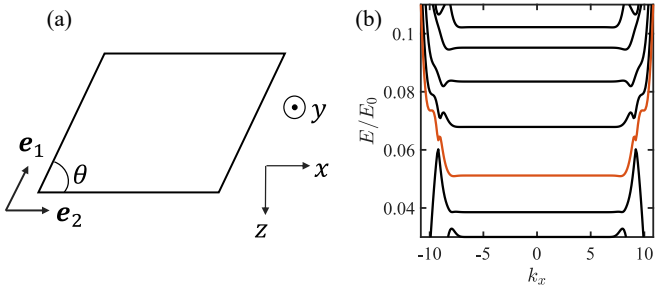


FIG. 6. (a) The geometry of the sample viewed from directly above. The directions of boundaries are indicated by unit vectors e_1 and e_2 with an angle θ . (b) Energy spectra of the Landau levels arising from Weyl orbits when $k_w = 2.1/l_B$ and other parameters are the same as Fig. 1 in the main text. We study the many-body physics on the Landau level marked by the red color, below which the total Chern number sums to zero.

TILTED MAGNETIC FIELD INDUCED TRANSITIONS

We now show that the transition from the CFL to the MR states can be induced by controlling the direction of the magnetic field, which is more experimentally accessible. Under the vertical magnetic field along y , the two ground states [colored red in Fig. 5(a)] exist in the same momentum sectors as the 2D CFL for ten electrons (see Appendix D). The structure factor $S(\mathbf{q})$ demonstrates a circle of peaks near $|\mathbf{q}| = 2k_F$ [Fig. 5(b)], characteristic of the CFL. We then tilt the magnetic field such that the magnetic field attains a nonzero x component, i.e., $\mathbf{B} = (B_x, B_y, 0)$. When $B_x/B_y = 1/25$, we see that the ground states become the MR states, confirmed by the many-body energy spectrum [Fig. 5(c)] and the particle entanglement spectrum [Fig. 5(d)], where the number of states below the gap indicated by the red dashed line satisfies the MR counting rule. The transition is also attributed to the increase of the number of nodes in the single-particle wave function of the considered Landau level (see Appendix C).

CONCLUSION

In summary, we have demonstrated the existence of the CFL, MR and CDW phases and their transitions in a Weyl-orbit-based Landau level. The transition is caused by a significant change in the wave function of the Landau level states as the distance between two Weyl points varies. We also show that varying the direction of a magnetic field can induce the transition from the CFL to MR states, providing an experimentally accessible method for observing the transition. In future, we will study the

phase diagram under broader parameter ranges to investigate the possibility of other types of phase transitions, e.g., the $2k_F$ density wave instabilities due to gauge fluctuations [66]. The effect of Landau level mixing is also an interesting question, which is left for future work.

We thank Y.-B. Yang and S.-C. Ma for helpful discussions. This work is supported by the National Natural Science Foundation of China (Grant No. 12474265, 11974201) and Innovation Program for Quantum Science and Technology (Grant No. 2021ZD0301604). We also acknowledge the support by Center of High Performance Computing, Tsinghua University.

APPENDIX A: A WEYL SEMIMETAL UNDER A MAGNETIC FIELD

In this Appendix, we will review how Weyl orbits arise in a Weyl semimetal under a magnetic field [12, 27] and show single-particle energy spectra of the Landau level based on Weyl orbits.

We follow Fig. 1(a) in the main text to schematically demonstrate how an electron evolves in a Weyl semimetal under a magnetic field. Specifically, starting from the projection of a Weyl point onto one surface, say the blue point on the top surface, an electron travels along the Fermi arc subjected to the magnetic field. At the end of the Fermi arc, a red point, it tunnels to the bottom surface through the Weyl point and then moves along the Fermi arc to the blue point. Subsequently, it tunnels back to the top surface, forming a closed loop called a Weyl orbit.

The Weyl orbit gives rise to Landau levels, as shown in Fig. 6(b), where we take OBCs in the z direction and PBCs in the x direction so that k_x is a good quantum number. In this paper, we study the many-body physics on the Landau level highlighted by the red color, given that the total Chern number below it sums to zero. Note that for numerical calculations, we choose the Landau gauge $\mathbf{A} = (Bz, 0, 0)$ for the magnetic field $\mathbf{B} = (0, B, 0)$. Since we focus on the many-body bulk physics, we use the following functions as a basis by considering a system that is infinite along z ,

$$\begin{aligned} \phi_{m,h}(y, z) &= \frac{1}{\sqrt{\sqrt{\pi}2^m m! l_B}} \sqrt{\frac{2}{L_y}} \exp \left[-\frac{(z - z_0)^2}{2l_B^2} \right] \\ &\quad \mathcal{H}_m \left(\frac{z - z_0}{l_B} \right) \sin \left[\frac{h\pi}{L_y} \left(y + \frac{L_y}{2} \right) \right], \end{aligned} \quad (A1)$$

where m takes non-negative integer values, h takes positive integer values, $l_B = \sqrt{\hbar/(eB)}$ is the magnetic length, L_y is the thickness of the sample in the y direction, $z_0 = -k_x l_B^2$ is the guiding center, and \mathcal{H}_m is the Hermite polynomial.

APPENDIX B: CONSTRUCTION OF THE MANY-BODY HAMILTONIAN

In this Appendix, we will show how to construct the interacting Hamiltonian (3) in the main text and present the procedure to arrive at the 2D Brillouin zone.

In this paper, we consider a parallelogram geometry in the horizontal plane described by unit vectors \mathbf{e}_1 and \mathbf{e}_2 with an angle $\theta = \pi/3$ as shown in Fig. 6(a). The system's lengths along \mathbf{e}_1 and \mathbf{e}_2 are L_1 and L_2 , respectively. In the study of the many-body physics of the half-filled Landau level in the main text, we take OBCs along y and PBCs along \mathbf{e}_1 and \mathbf{e}_2 . The single-particle state on the Landau level we investigate is a spinor $\Psi_j = (\psi_{j,0}, \psi_{j,1})^T$ where

$$\psi_{j,\sigma} = \sum_{m,h} c_{m,h,\sigma} \tilde{\phi}_{m,h,j} \quad (B1)$$

with $\sigma = 0, 1$ and $c_{m,h,\sigma}$ obtained by numerically diagonalizing the single-particle Weyl semimetal Hamiltonian in the basis (A1). Here

$$\begin{aligned} \tilde{\phi}_{m,h,j}(\mathbf{r}) &= \frac{1}{\sqrt{\sqrt{\pi} 2^m m! l_B L_2}} \sqrt{\frac{2}{L_y}} \sum_{n=-\infty}^{+\infty} \exp \left[i \frac{2\pi}{L_2} (j + nN_\phi) (x - \frac{\pi \cos \theta}{L_2 \sin \theta} (j + nN_\phi) l_B^2) \right] \\ &\quad \exp \left[-\frac{(z - z_n)^2}{2l_B^2} \right] \mathcal{H}_m \left(\frac{z - z_n}{l_B} \right) \sin \left[\frac{h\pi}{L_y} \left(y + \frac{L_y}{2} \right) \right] \end{aligned} \quad (B2)$$

is a remedied form of (A1) for consistency with PBCs, where $z_n = -2\pi j l_B^2 / L_2 - nL_1 \sin \theta$, $j = 0, \dots, N_\phi - 1$ with N_ϕ being the degeneracy of the Landau level. To be explicit, it is easy to obtain

$$\tilde{\phi}_{m,h,j}(\mathbf{r} + L_1 \mathbf{e}_1) = e^{i2\pi N_\phi x / L_2} e^{i2\pi^2 \cos \theta N_\phi^2 l_B^2 / (L_2^2 \sin \theta)} \tilde{\phi}_{m,h,j}(\mathbf{r}), \quad (B3)$$

$$\tilde{\phi}_{m,h,j}(\mathbf{r} + L_2 \mathbf{e}_2) = \tilde{\phi}_{m,h,j}(\mathbf{r}). \quad (B4)$$

The magnetic translation operator is $\mathcal{T}(\mathbf{d}) = e^{i\mathbf{d} \cdot \mathbf{K}}$ where $\mathbf{K} = -i\nabla + e\mathbf{A} - e\mathbf{B} \times \mathbf{r}$ for $\mathbf{d} = (d_x, 0, d_z)$. We can also derive

$$\mathcal{T}(L_1 \mathbf{e}_1) = e^{-i2\pi N_\phi x / L_2} e^{-i2\pi^2 \cos \theta N_\phi^2 l_B^2 / (L_2^2 \sin \theta)} T(L_1 \mathbf{e}_1), \quad (B5)$$

and

$$\mathcal{T}(L_2 \mathbf{e}_2) = T(L_2 \mathbf{e}_2) \quad (B6)$$

where $T(\mathbf{d})$ is the ordinary translation operator. As a result, the wave functions in Eq. (B2) satisfy

$$\mathcal{T}(L_1 \mathbf{e}_1) \tilde{\phi}_{m,h,j}(\mathbf{r}) = \tilde{\phi}_{m,h,j}(\mathbf{r}) \quad (B7)$$

$$\mathcal{T}(L_2 \mathbf{e}_2) \tilde{\phi}_{m,h,j}(\mathbf{r}) = \tilde{\phi}_{m,h,j}(\mathbf{r}), \quad (B8)$$

which is consistent with the PBCs. In the derivation of (B5) and (B6), we have used the Zassenhaus formula that $e^{A+B} = e^A e^B e^{-[A,B]/2}$ when $[[A, B], A] = [[A, B], B] = 0$ with $[A, B]$ being the commutator of A and B .

By projecting the Coulomb interaction onto one Landau level, we obtain the interacting Hamiltonian

$$\hat{H}_I = \sum_{j_1, j_2, j_3, j_4=0}^{N_\phi-1} B_{j_1 j_2 j_3 j_4} \hat{a}_{j_1}^\dagger \hat{a}_{j_2}^\dagger \hat{a}_{j_3} \hat{a}_{j_4}, \quad (B9)$$

where $\hat{a}_{j_\mu}^\dagger$ (\hat{a}_{j_μ}) is the creation (annihilation) operator of the single-particle state Ψ_j in the Landau level under investigation. The coefficients

$$B_{j_1 j_2 j_3 j_4} = \sum_{\sigma_1 \sigma_2} \sum_{m_{1,2,3,4} h_{1,2,3,4}} c_{m_1, h_1, \sigma_1}^* c_{m_2, h_2, \sigma_2}^* c_{m_3, h_3, \sigma_2} c_{m_4, h_4, \sigma_1} A_{j_1 j_2 j_3 j_4}^{m_1 m_2 m_2 m_3 m_3 m_4 h_4}, \quad (B10)$$

where

$$\begin{aligned} A_{j_1 j_2 j_3 j_4}^{m_1 m_2 m_2 m_3 h_3 m_4 h_4} &= \frac{e^2}{4\pi\epsilon} \frac{1}{2L_x L_z \sin \theta} \sum_{q_x, q_z, s, t}^{\prime} \frac{2\pi}{q} F(\mathbf{q}) G_1(\mathbf{q}) G_2(\mathbf{q}) e^{i \frac{2\pi s(j_3 - j_1)}{N_\phi}} \\ &\quad \times \delta_{q_x, \frac{2\pi}{L_x} t} \delta_{q_z, \frac{2\pi}{L_z \sin \theta} s - \frac{2\pi \cos \theta}{L_x \sin \theta} t} \delta'_{t, j_1 - j_4} \delta'_{j_1 + j_2, j_3 + j_4}, \end{aligned} \quad (B11)$$

with

$$F(\mathbf{q}) = \int_{-L_y/2}^{L_y/2} \int_{-L_y/2}^{L_y/2} dy_1 dy_2 \left(\frac{2}{L_y}\right)^2 \sin\left[\frac{h_1\pi}{L_y}(y_1 + \frac{L_y}{2})\right] \sin\left[\frac{h_4\pi}{L_y}(y_1 + \frac{L_y}{2})\right] \sin\left[\frac{h_2\pi}{L_y}(y_2 + \frac{L_y}{2})\right] \sin\left[\frac{h_3\pi}{L_y}(y_2 + \frac{L_y}{2})\right] e^{-q|y_1 - y_2|}, \quad (\text{B12})$$

$$G_1(\mathbf{q}) = \sqrt{\frac{\min(m_1, m_4)!}{\max(m_1, m_4)!}} e^{-q^2 l_B^2/4} \left[\frac{\text{sgn}(m_1 - m_4) q_x + iq_z}{\sqrt{2}} l_B \right]^{m_1 - m_4} L_{\min(m_1, m_4)}^{(|m_1 - m_4|)}\left(\frac{q^2 l_B^2}{2}\right), \quad (\text{B13})$$

$$G_2(\mathbf{q}) = \sqrt{\frac{\min(m_2, m_3)!}{\max(m_2, m_3)!}} e^{-q^2 l_B^2/4} \left[\frac{-\text{sgn}(m_2 - m_3) q_x - iq_z}{\sqrt{2}} l_B \right]^{m_2 - m_3} L_{\min(m_2, m_3)}^{(|m_2 - m_3|)}\left(\frac{q^2 l_B^2}{2}\right). \quad (\text{B14})$$

Here $\mathbf{q} = (q_x, q_z)$, $q = |\mathbf{q}|$, $L_{\min(m_1, m_4)}^{(|m_1 - m_4|)}$ is the Laguerre polynomial and s, t take integer values. The detailed derivation can be found in the Appendix of Ref. [48].

In the following, we will follow Ref. [71] to construct a 2D Brillouin zone for Landau level states, i.e., rewrite the Hamiltonian (B9) as

$$\hat{H}_I = \sum_{\mathbf{k}_1, \mathbf{k}_2, \mathbf{k}_3, \mathbf{k}_4} C_{\mathbf{k}_1 \mathbf{k}_2 \mathbf{k}_3 \mathbf{k}_4} \hat{c}_{\mathbf{k}_1}^\dagger \hat{c}_{\mathbf{k}_2}^\dagger \hat{c}_{\mathbf{k}_3} \hat{c}_{\mathbf{k}_4}, \quad (\text{B15})$$

where $\hat{c}_{\mathbf{k}}$ ($\hat{c}_{\mathbf{k}}^\dagger$) is the annihilation (creation) operator of the single-particle state with two labels k_1, k_2 for each \mathbf{k} with $k_i = 0, 1, \dots, N_i - 1$ for $i = 1, 2$ and $N_1 \cdot N_2 = N_\phi$. It is nothing more than a basis transformation. We define

$$\hat{c}_{\mathbf{k}}^\dagger = \frac{1}{\sqrt{N_1}} \sum_{n=0}^{N_1-1} e^{i2\pi n k_1 / N_1} \hat{a}_{j=n N_2 + k_2}^\dagger, \quad (\text{B16})$$

and utilizing the explicit form of $\tilde{\phi}_{m,h,j}(\mathbf{r})$ in (B2), we find

$$\mathcal{T}(L_1 \mathbf{e}_1 / N_1) \hat{c}_{\mathbf{k}}^\dagger |0\rangle = e^{i2\pi k_1 / N_1} \hat{c}_{\mathbf{k}}^\dagger |0\rangle, \quad (\text{B17})$$

$$\mathcal{T}(L_2 \mathbf{e}_2 / N_2) \hat{c}_{\mathbf{k}}^\dagger |0\rangle = e^{i2\pi k_2 / N_2} \hat{c}_{\mathbf{k}}^\dagger |0\rangle, \quad (\text{B18})$$

which is like the Bloch states of a 2D lattice system with $N_1 \times N_2$ unit cells and lattice constant $L_1/N_1, L_2/N_2$ in the \mathbf{e}_1 and \mathbf{e}_2 directions, respectively. We thus can construct a 2D Brillouin zone with Bloch wave vectors $\mathbf{k} = k_1 \mathbf{g}_1 + k_2 \mathbf{g}_2$, where $\mathbf{g}_i \cdot \mathbf{e}_j = \delta_{ij} 2\pi / L_i$ with δ_{ij} being the Kronecker delta function. The reciprocal lattice vector $\mathbf{G}_1 = N_1 \mathbf{g}_1, \mathbf{G}_2 = N_2 \mathbf{g}_2$, so $|\mathbf{G}_1| = |\mathbf{G}_2|$ when $L_1/N_1 = L_2/N_2$, corresponding to a hexagonal Brillouin zone when $\theta = \pi/3$. We can easily find that

$$C_{\mathbf{k}_1 \mathbf{k}_2 \mathbf{k}_3 \mathbf{k}_4} = \frac{1}{N_1^2} \sum_{n_1, n_2, n_3, n_4=0}^{N_1-1} e^{-i2\pi(n_1 k_{1,1} + n_2 k_{2,1} - n_3 k_{3,1} - n_4 k_{4,1}) / N_1} A_{n_1 N_2 + k_{1,2}, n_2 N_2 + k_{2,2}, n_3 N_2 + k_{3,2}, n_4 N_2 + k_{4,2}}, \quad (\text{B19})$$

where $k_{i,j}$ stands for the k_j component of \mathbf{k}_i .

APPENDIX C: REAL-SPACE WAVE FUNCTIONS IN A LANDAU LEVEL ARISING FROM WEYL ORBITS

In this Appendix, we will display the real-space wave functions in a Weyl-orbit-based Landau level that we focus on to elucidate the mechanism of the transitions between the many-body phases in the main text.

We first show that wave functions in the Landau level

are mainly localized near top and bottom surfaces. Without loss of generality, we consider $k_x = 0$ such that the guiding center is located at $z_0 = 0$. The density of the single-particle wave function $\mathbf{f} = (f_0, f_1)$ along y is given by

$$\rho_y = \int dz (|f_0(y, z)|^2 + |f_1(y, z)|^2), \quad (\text{C1})$$

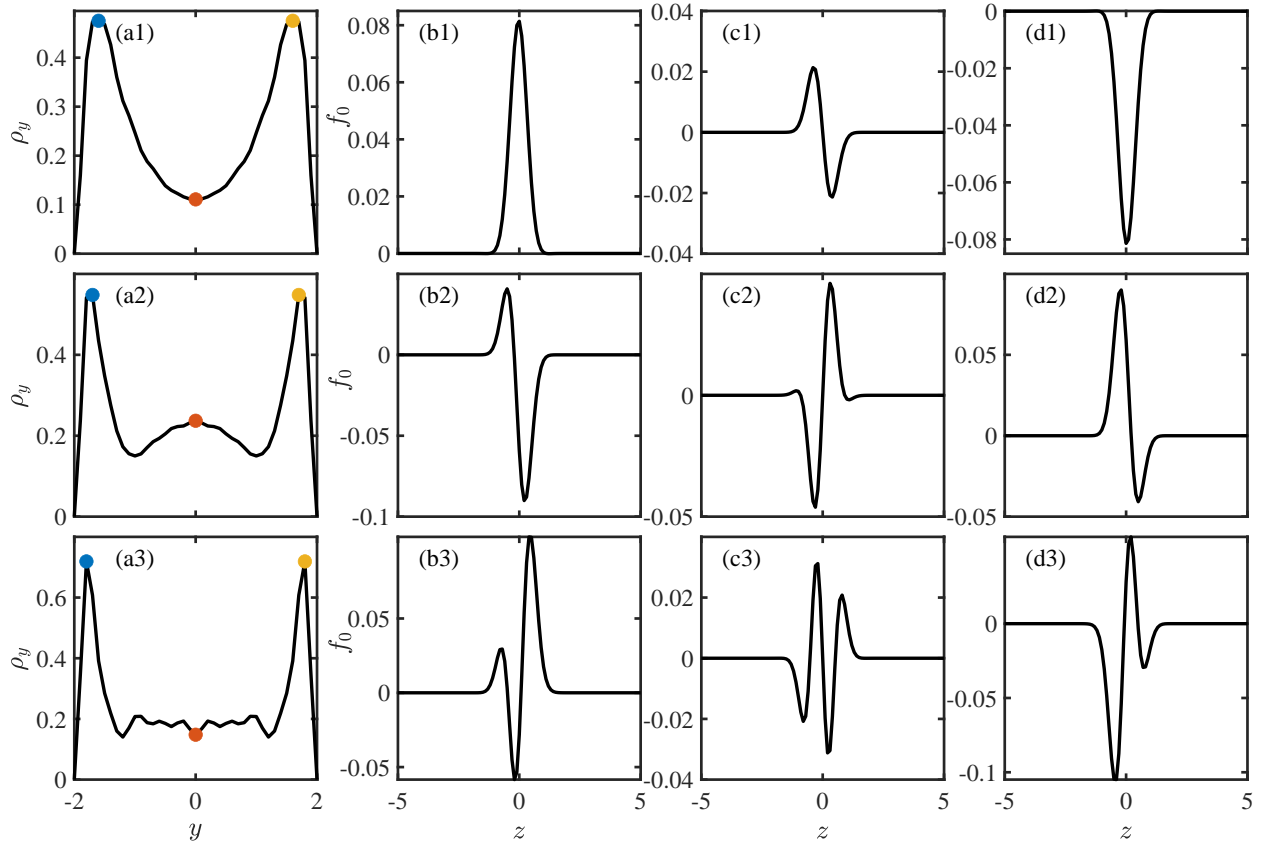


FIG. 7. (a1)-(a3) The electron density distribution ρ_y with respect to y . The real-space wave function $f_0(y_0, z)$ versus z (b1)-(b3) near a bottom surface, (c1)-(c3) deep in the bulk, (d1)-(d3) near a top surface, at a fixed y_0 indicated by the blue, red, and yellow points in (a), respectively. In the first, second, and third rows, $k_w = 1.4/l_B$, $k_w = 2.1/l_B$, and $k_w = 2.7/l_B$, respectively. Other parameters are the same as Fig. 1 in the main text.

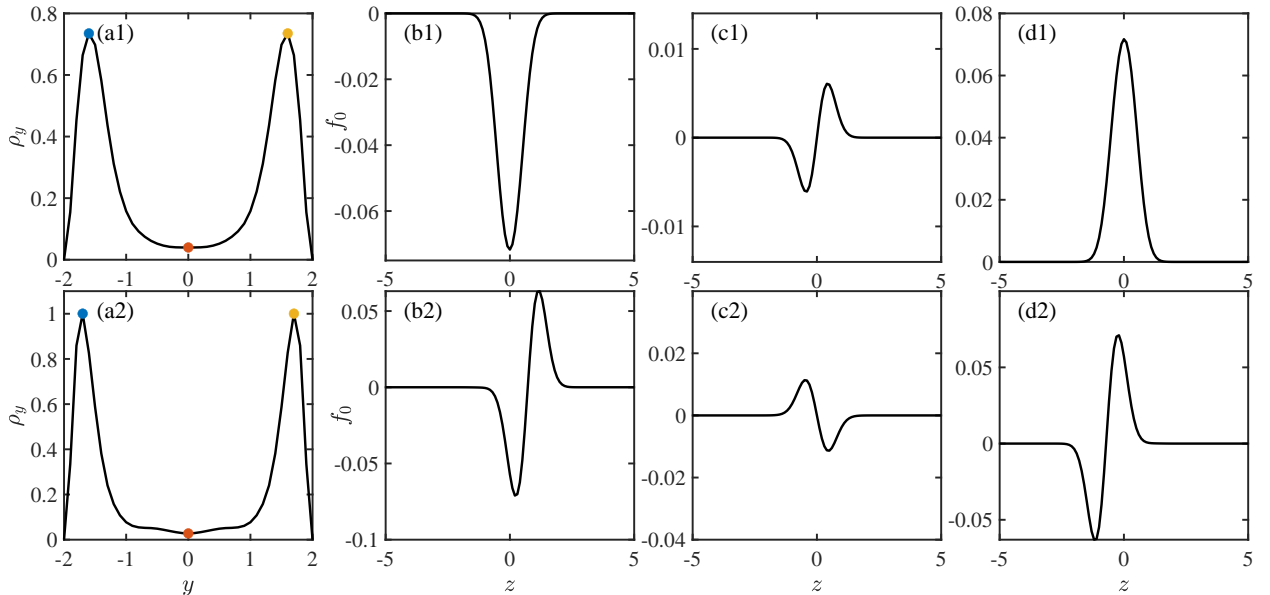


FIG. 8. The same as Fig. 7 except that we take the parameters the same as Fig. 5 in the main text with a vertical magnetic field in the first row and a tilted magnetic field in the second row.

where the wave function is described by

$$f_\sigma(y, z) = \sum_{m,h} c_{m,h,\sigma} \phi_{m,h}(y, z), \quad (\text{C2})$$

with $\phi_{m,h}$ being the wave function in Eq. (A1). The density profiles shown in Figs. 7(a1)-7(a3) imply that the states are mainly distributed near top and bottom surfaces.

To demonstrate why the phase transition occurs as the distance between Weyl points is varied, we plot $f_0(y, z)$ (similarly for f_1) with respect to z at a fixed y (near top and bottom surfaces) in Fig. 7 for different k_w 's.

Figures 7(b1) and (d1) illustrate that at $k_w = 1.4/l_B$, the wave functions near the surfaces, where the electron density is concentrated [see Fig. 7(a)], exhibit no nodes, similar to the lowest Landau level in 2D. Thus, the CFL is favored. Note that although the wave function in the bulk hosts one node [see Fig. 7(c1)], it plays a much less important role because the electron density deep in the bulk is small [see Fig. 7(a)].

As we increase k_w to $2.1/l_B$, we see from Figs. 7(b2) and 7(d2) that the wave function exhibits one node akin to the first excited Landau level in 2D, suggesting that the MR states are favorable.

At $k_w = 2.7/l_B$, two nodes show up in the wave function on the surfaces [see Figs. 7(b3) and 7(d3)], supporting the CDW [60–62].

Similarly, when we tune the magnetic field from a vertical one to a tilted one, we find that the wave functions on the surfaces develop a node as shown in Fig. 8, leading to the transition from the CFL to MR states.

APPENDIX D: MANY-BODY ENERGY SPECTRUM OF THE CFL AND MR STATES IN 2D

In this Appendix, we show the many-body energy spectrum of the half-filled lowest and first excited Landau level in a 2D electron gas with Coulomb interactions, which host CFL (Fig. 9) and MR phases (Fig. 10), respectively. Here we project the Coulomb interaction onto a single Landau level. In the main text, we have compared the many-body energy spectra in Weyl semimetals with those in 2D electron gases, suggesting that the found phases are CFL or MR states.

APPENDIX E: GUIDING CENTER COORDINATE OPERATOR

In this Appendix, we will follow Ref. [54] to provide a brief review on the guiding center coordinate operator.

For simplicity, we consider a 2D electron gas under a

magnetic field with the Hamiltonian

$$\hat{H} = \frac{1}{2m}(\hat{\pi}_x^2 + \hat{\pi}_y^2), \quad (\text{E1})$$

where $\hat{\pi}_a = \hat{p}_a + e\hat{A}_a$ with $a = x, y$ and $\hat{\mathbf{A}}$ being the vector potential. We write the real space coordinate operator \hat{r}^a as

$$\hat{r}^a = \hat{R}^a + \hat{\tilde{R}}^a, \quad (\text{E2})$$

where $\hat{\tilde{R}}^a := (l_B^2/\hbar) \sum_b \epsilon^{ab} \hat{\pi}_b$, with ϵ^{ab} being the anti-symmetric Levi-Civita symbol. Physically, $\hat{\mathbf{R}} = (\hat{R}^x, \hat{R}^y)$ is the guiding center or origin of the cyclotron motion of the electron under the magnetic field, and $\hat{\tilde{\mathbf{R}}} = (\hat{\tilde{R}}^a, \hat{\tilde{R}}^b)$ is the coordinate relative to the guiding center during the cyclotron motion. Based on the fact that $[\hat{\pi}_x, \hat{\pi}_y] = -i\hbar^2/l_B^2$, we obtain the following commutation rules:

$$\begin{aligned} [\hat{R}^a, \hat{R}^b] &= 0, \\ [\hat{R}^a, \hat{R}^b] &= \epsilon^{ab} il_B^2, \\ [\hat{\tilde{R}}^a, \hat{\tilde{R}}^b] &= -\epsilon^{ab} il_B^2. \end{aligned} \quad (\text{E3})$$

We see that \hat{R}^a and $\hat{\tilde{R}}^a$ are two independent sets of canonical conjugate variables so that we can define two sets of ladder operators:

$$\hat{b}^\dagger = \frac{1}{\sqrt{2l_B}}(\hat{R}^x - i\hat{R}^y), \quad (\text{E4})$$

$$\hat{b} = \frac{1}{\sqrt{2l_B}}(\hat{R}^x + i\hat{R}^y), \quad (\text{E5})$$

and

$$\hat{f}^\dagger = \frac{1}{\sqrt{2l_B}}(\hat{\tilde{R}}^x + i\hat{\tilde{R}}^y), \quad (\text{E6})$$

$$\hat{f} = \frac{1}{\sqrt{2l_B}}(\hat{\tilde{R}}^x - i\hat{\tilde{R}}^y). \quad (\text{E7})$$

The Hamiltonian (E1) can thus be written in term of \hat{f} and \hat{f}^\dagger as

$$\hat{H} = \hbar\omega(\hat{f}^\dagger \hat{f} + \frac{1}{2}) \quad (\text{E8})$$

with $\omega = eB/m$. The n th eigenstate in the m th Landau level corresponding to the energy $E_m = \hbar\omega(m + 1/2)$ is given by

$$|m, n\rangle = \frac{(\hat{f}^\dagger)^m (\hat{b}^\dagger)^n}{\sqrt{n!m!}} |0\rangle, \quad (\text{E9})$$

which shows that $\hat{\tilde{R}}^a$ controls the transition between different Landau levels and \hat{R}^a governs the dynamics within a single Landau level. This indicates that only the guiding center operator \hat{R}^a comes into effect after the projection onto a specific Landau level.

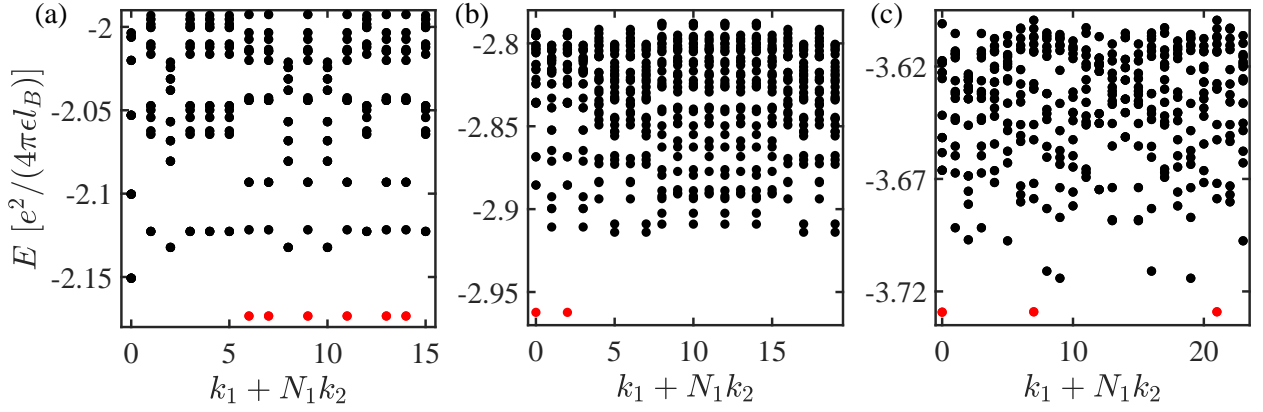


FIG. 9. The many-body energy spectra of the half-filled lowest Landau level in a 2D electron gas with Coulomb interactions for (a) eight, (b) ten, and (c) twelve electrons, which indicate the paradigmatic CFL phase. The lowest energy states are colored red.

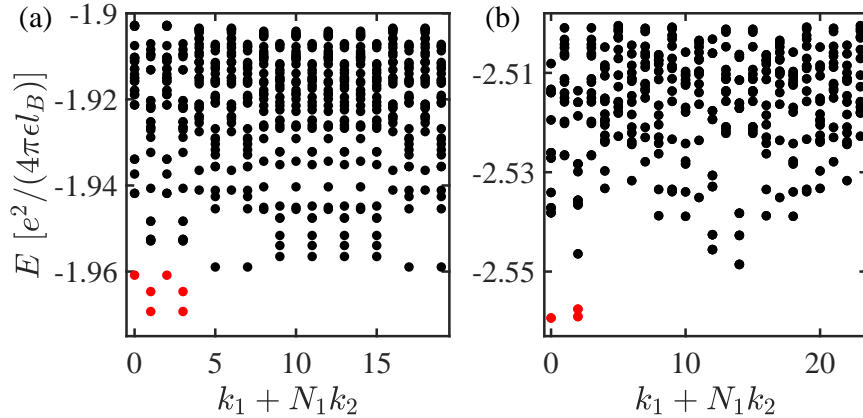


FIG. 10. The many-body energy spectra of the half-filled first excited Landau level in a 2D electron gas with Coulomb interactions for (a) ten and (b) twelve electrons, hosting the MR states, which are colored red.

In the main text, we calculate the guiding center static structure factor

$$S(\mathbf{q}) = \frac{\langle \bar{\rho}(\mathbf{q})\bar{\rho}(-\mathbf{q}) \rangle}{n_e} - \frac{\langle \bar{\rho}(0) \rangle^2}{n_e} \quad (\text{E10})$$

using the guiding center density operator $\bar{\rho}(\mathbf{q}) = \sum_i e^{i\mathbf{q} \cdot \hat{\mathbf{R}}_i}$. Under the single Landau level projection, $\rho(\mathbf{q}) = L_n(q^2 l_B^2/2) e^{-q^2 l_B^2/4} \bar{\rho}(\mathbf{q})$ [72], where L_n is the Laguerre polynomial, and $\rho(\mathbf{q}) = \sum_i e^{i\mathbf{q} \cdot \hat{\mathbf{r}}_i}$ is the ordinary density operator, which is useful for the derivation of the second-quantization form of $\rho(\mathbf{q})$ for numerical evaluations of $S(\mathbf{q})$.

- [3] N. P. Armitage, E. J. Mele, and A. Vishwanath, Weyl and Dirac semimetals in three-dimensional solids, *Rev. Mod. Phys.* **90**, 015001 (2018).
- [4] Y. Xu, Topological gapless matters in three-dimensional ultracold atomic gases, *Front. Phys.* **14**, 43402 (2019).
- [5] B. Q. Lv, T. Qian, and H. Ding, Experimental perspective on three-dimensional topological semimetals, *Rev. Mod. Phys.* **93**, 025002 (2021).
- [6] X. Wan, A. M. Turner, A. Vishwanath, and S. Y. Savrasov, Topological semimetal and Fermi-arc surface states in the electronic structure of pyrochlore iridates, *Phys. Rev. B* **83**, 205101 (2011).
- [7] K.-Y. Yang, Y.-M. Lu, and Y. Ran, Quantum Hall effects in a Weyl semimetal: Possible application in pyrochlore iridates, *Phys. Rev. B* **84**, 075129 (2011).
- [8] A. A. Burkov and L. Balents, Weyl semimetal in a topological insulator multilayer, *Phys. Rev. Lett.* **107**, 127205 (2011).
- [9] G. Xu, H. Weng, Z. Wang, X. Dai, and Z. Fang, Chern semimetal and the quantized anomalous Hall effect in HgCr_2Se_4 , *Phys. Rev. Lett.* **107**, 186806 (2011).
- [10] W. Witczak-Krempa, M. Knap, and D. Abanin, Interacting Weyl semimetals: Characterization via the topological Hamiltonian and its breakdown, *Phys. Rev. Lett.*

* yongxuphy@tsinghua.edu.cn

- [1] S. Jia, S.-Y. Xu, and M. Z. Hasan, Weyl semimetals, Fermi arcs and chiral anomalies, *Nat. Mater.* **15**, 1140 (2016).
- [2] A. A. Burkov, Topological semimetals, *Nat. Mater.* **15**, 1145 (2016).

113, 136402 (2014).

[11] S.-K. Jian and H. Yao, Correlated double-Weyl semimetals with Coulomb interactions: Possible applications to HgCr_2Se_4 and SrSi_2 , *Phys. Rev. B* **92**, 045121 (2015).

[12] A. C. Potter, I. Kimchi, and A. Vishwanath, Quantum oscillations from surface Fermi arcs in Weyl and Dirac semimetals, *Nat Commun* **5**, 5161 (2014).

[13] E. J. Bergholtz, Z. Liu, M. Trescher, R. Moessner, and M. Udagawa, Topology and interactions in a frustrated slab: Tuning from Weyl semimetals to $C > 1$ fractional Chern insulators, *Phys. Rev. Lett.* **114**, 016806 (2015).

[14] H. Weng, C. Fang, Z. Fang, B. A. Bernevig, and X. Dai, Weyl semimetal phase in noncentrosymmetric transition-metal monophosphides, *Phys. Rev. X* **5**, 011029 (2015).

[15] S. A. Yang, H. Pan, and F. Zhang, Chirality-dependent Hall effect in Weyl semimetals, *Phys. Rev. Lett.* **115**, 156603 (2015).

[16] C.-Z. Chen, J. Song, H. Jiang, Q.-f. Sun, Z. Wang, and X. C. Xie, Disorder and metal-insulator transitions in Weyl semimetals, *Phys. Rev. Lett.* **115**, 246603 (2015).

[17] Y. Xu, F. Zhang, and C. Zhang, Structured Weyl points in spin-orbit coupled fermionic superfluids, *Phys. Rev. Lett.* **115**, 265304 (2015).

[18] A. A. Soluyanov, D. Gresch, Z. Wang, Q. Wu, M. Troyer, X. Dai, and B. A. Bernevig, Type-II Weyl semimetals, *Nature* **527**, 495 (2015).

[19] T. Morimoto and N. Nagaosa, Weyl Mott insulator, *Sci Rep* **6**, 19853 (2016).

[20] J. H. Pixley, D. A. Huse, and S. Das Sarma, Rare-region-induced avoided quantum criticality in disordered three-dimensional Dirac and Weyl semimetals, *Phys. Rev. X* **6**, 021042 (2016).

[21] H. Ishizuka, T. Hayata, M. Ueda, and N. Nagaosa, Emergent electromagnetic induction and adiabatic charge pumping in noncentrosymmetric Weyl semimetals, *Phys. Rev. Lett.* **117**, 216601 (2016).

[22] J. Carlström and E. J. Bergholtz, Strongly interacting Weyl semimetals: Stability of the semimetallic phase and emergence of almost free fermions, *Phys. Rev. B* **98**, 241102 (2018).

[23] Y.-B. Yang, T. Qin, D.-L. Deng, L.-M. Duan, and Y. Xu, Topological amorphous metals, *Phys. Rev. Lett.* **123**, 076401 (2019).

[24] C. Wang, L. Gioia, and A. A. Burkov, Fractional quantum Hall effect in Weyl semimetals, *Phys. Rev. Lett.* **124**, 096603 (2020).

[25] X. Yao, J. Gaudet, R. Verma, D. E. Graf, H.-Y. Yang, F. Bahrami, R. Zhang, A. A. Aczel, S. Subedi, D. H. Torchinsky, J. Sun, A. Bansil, S.-M. Huang, B. Singh, P. Blaha, P. Nikolić, and F. Tafti, Large topological Hall effect and spiral magnetic order in the Weyl semimetal smalsi, *Phys. Rev. X* **13**, 011035 (2023).

[26] S. Nandy, C. Lane, and J.-X. Zhu, Quantum Hall effect in a Weyl-Hubbard model: Interplay between topology and correlation, *Phys. Rev. B* **109**, 085111 (2024).

[27] C. M. Wang, H.-P. Sun, H.-Z. Lu, and X. C. Xie, 3D quantum Hall effect of Fermi arcs in topological semimetals, *Phys. Rev. Lett.* **119**, 136806 (2017).

[28] C. Zhang, A. Narayan, S. Lu, J. Zhang, H. Zhang, Z. Ni, X. Yuan, Y. Liu, J.-H. Park, E. Zhang, W. Wang, S. Liu, L. Cheng, L. Pi, Z. Sheng, S. Sanvito, and F. Xiu, Evolution of Weyl orbit and quantum Hall effect in Dirac semimetal Cd_3As_2 , *Nat. Commun.* **8**, 1272 (2017).

[29] M. Uchida, Y. Nakazawa, S. Nishihaya, K. Akiba, M. Kriener, Y. Kozuka, A. Miyake, Y. Taguchi, M. Tokunaga, N. Nagaosa, Y. Tokura, and M. Kawasaki, Quantum Hall states observed in thin films of Dirac semimetal Cd_3As_2 , *Nat. Commun.* **8**, 2274 (2017).

[30] T. Schumann, L. Galletti, D. A. Kealhofer, H. Kim, M. Goyal, and S. Stemmer, Observation of the quantum Hall effect in confined films of the three-dimensional Dirac semimetal Cd_3As_2 , *Phys. Rev. Lett.* **120**, 016801 (2018).

[31] C. Zhang, Y. Zhang, X. Yuan, S. Lu, J. Zhang, A. Narayan, Y. Liu, H. Zhang, Z. Ni, R. Liu, E. S. Choi, A. Suslov, S. Sanvito, L. Pi, H.-Z. Lu, A. C. Potter, and F. Xiu, Quantum Hall effect based on Weyl orbits in Cd_3As_2 , *Nature* **565**, 331 (2019).

[32] H.-Z. Lu, 3D quantum Hall effect, *Nat. Sci. Rev.* **6**, 208 (2019).

[33] H. Li, H. Liu, H. Jiang, and X. C. Xie, 3D quantum Hall effect and a global picture of edge states in Weyl semimetals, *Phys. Rev. Lett.* **125**, 036602 (2020).

[34] S. Nishihaya, M. Uchida, Y. Nakazawa, M. Kriener, Y. Taguchi, and M. Kawasaki, Intrinsic coupling between spatially-separated surface Fermi-arcs in Weyl orbit quantum Hall states, *Nat. Commun.* **12**, 2572 (2021).

[35] R. Chen, T. Liu, C. M. Wang, H.-Z. Lu, and X. C. Xie, Field-tunable one-sided higher-order topological hinge states in Dirac semimetals, *Phys. Rev. Lett.* **127**, 066801 (2021).

[36] C. Zhang, Y. Zhang, H.-Z. Lu, X. C. Xie, and F. Xiu, Cycling Fermi arc electrons with Weyl orbits, *Nat. Rev. Phys.* **3**, 660 (2021).

[37] S. Li, C. M. Wang, Z. Z. Du, F. Qin, H.-Z. Lu, and X. C. Xie, 3D quantum Hall effects and nonlinear Hall effect, *npj Quantum Mater.* **6**, 1 (2021).

[38] M. Chang, Y. Ge, and L. Sheng, Generalization of the theory of three-dimensional quantum Hall effect of Fermi arcs in Weyl semimetal, *Chin. Phys. B* **31**, 057304 (2022).

[39] F. Xiong, C. Honerkamp, D. M. Kennes, and T. Nag, Understanding the three-dimensional quantum Hall effect in generic multi-Weyl semimetals, *Phys. Rev. B* **106**, 045424 (2022).

[40] X. Zhang, Y. Lee, V. Kakani, K. Yang, K. Cho, and X. Shi, Two types of three-dimensional quantum Hall effects in multilayer WTe_2 , *Phys. Rev. B* **107**, 245410 (2023).

[41] J.-H. Wang and Y. Xu, Three-dimensional quantum Hall effect in topological amorphous metals (2023), arXiv:2309.05990 [cond-mat].

[42] Y. Nakazawa, R. Kurihara, M. Miyazawa, S. Nishihaya, M. Kriener, M. Tokunaga, M. Kawasaki, and M. Uchida, Edge and bulk states in Weyl-orbit quantum Hall effect as studied by Corbino measurements, *J. Phys. Soc. Jpn.* **93**, 023706 (2024).

[43] T.-R. Qin, Z.-H. Chen, T.-X. Liu, F.-Y. Chen, H.-J. Duan, M.-X. Deng, and R.-Q. Wang, Quantum Hall effect in topological Dirac semimetals modulated by the Lifshitz transition of the Fermi arc surface states, *Phys. Rev. B* **109**, 125111 (2024).

[44] Z.-X. Kong, Z.-Z. Xiong, W.-J. Wang, H.-J. Duan, M. Yang, M.-X. Deng, and R.-Q. Wang, Photon-assisted extrinsic Weyl orbits and three-dimensional quantum Hall effect in surface-doped topological Dirac semimetals, *Phys. Rev. B* **110**, 075136 (2024).

[45] M. Chang and R. Ma, Anisotropic three-dimensional quantum Hall effect in topological nodal-line semimetals,

Phys. Rev. B **110**, 045413 (2024).

[46] X. Zhang, Q. Wei, M. Peng, W. Deng, J. Lu, X. Huang, S. Jia, M. Yan, Z. Liu, and G. Chen, Observation of 3D acoustic quantum Hall states, *Science Bulletin* **69**, 2187 (2024).

[47] L. Ye, Q. Wang, Z. Fu, H. He, X. Huang, M. Ke, J. Lu, W. Deng, and Z. Liu, Hinge modes of surface arcs in a synthetic Weyl phononic crystal, *Phys. Rev. Lett.* **133**, 126602 (2024).

[48] J.-H. Wang, Y.-B. Yang, and Y. Xu, Fractional quantum Hall effect based on Weyl orbits, *Phys. Rev. B* **111**, 045108 (2025).

[49] J. Jain, Microscopic theory of the fractional quantum Hall effect, *Adv. Phys.* **41**, 105 (1992).

[50] H. L. Stormer, D. C. Tsui, and A. C. Gossard, The fractional quantum Hall effect, *Rev. Mod. Phys.* **71**, S298 (1999).

[51] H. L. Stormer, Nobel lecture: The fractional quantum Hall effect, *Rev. Mod. Phys.* **71**, 875 (1999).

[52] G. Murthy and R. Shankar, Hamiltonian theories of the fractional quantum Hall effect, *Rev. Mod. Phys.* **75**, 1101 (2003).

[53] T. H. Hansson, M. Hermanns, S. H. Simon, and S. F. Viefers, Quantum Hall physics: Hierarchies and conformal field theory techniques, *Rev. Mod. Phys.* **89**, 025005 (2017).

[54] J. K. Jain, *Composite Fermions* (Cambridge University Press, Cambridge, 2007).

[55] B. I. Halperin, P. A. Lee, and N. Read, Theory of the half-filled Landau level, *Phys. Rev. B* **47**, 7312 (1993).

[56] G. Moore and N. Read, Nonabelions in the fractional quantum Hall effect, *Nucl. Phys. B* **360**, 362 (1991).

[57] N. Read and E. Rezayi, Beyond paired quantum Hall states: Parafermions and incompressible states in the first excited Landau level, *Phys. Rev. B* **59**, 8084 (1999).

[58] C. Nayak, S. H. Simon, A. Stern, M. Freedman, and S. Das Sarma, Non-Abelian anyons and topological quantum computation, *Rev. Mod. Phys.* **80**, 1083 (2008).

[59] D. Yoshioka, B. I. Halperin, and P. A. Lee, Ground state of two-dimensional electrons in strong magnetic fields and 1/3 quantized Hall effect, *Phys. Rev. Lett.* **50**, 1219 (1983).

[60] E. H. Rezayi, F. D. M. Haldane, and K. Yang, Charge-density-wave ordering in half-filled high Landau levels, *Phys. Rev. Lett.* **83**, 1219 (1999).

[61] E. H. Rezayi and F. D. M. Haldane, Incompressible paired Hall state, stripe order, and the composite fermion liquid phase in half-filled Landau levels, *Phys. Rev. Lett.* **84**, 4685 (2000).

[62] F. D. M. Haldane, E. H. Rezayi, and K. Yang, Spontaneous breakdown of translational symmetry in quantum Hall systems: Crystalline order in high Landau levels, *Phys. Rev. Lett.* **85**, 5396 (2000).

[63] J. Dong, J. Wang, P. J. Ledwith, A. Vishwanath, and D. E. Parker, Composite Fermi liquid at zero magnetic field in twisted MoTe₂, *Phys. Rev. Lett.* **131**, 136502 (2023).

[64] H. Goldman, A. P. Reddy, N. Paul, and L. Fu, Zero-field composite Fermi liquid in twisted semiconductor bilayers, *Phys. Rev. Lett.* **131**, 136501 (2023).

[65] S. D. Geraedts, J. Wang, E. H. Rezayi, and F. D. M. Haldane, Berry phase and model wave function in the half-filled Landau level, *Phys. Rev. Lett.* **121**, 147202 (2018).

[66] S.-K. Jian and Z. Zhu, 2k_F density wave instability of composite Fermi liquid, *Phys. Rev. Res.* **2**, 033414 (2020).

[67] S. D. Geraedts, M. P. Zaletel, R. S. K. Mong, M. A. Metlitski, A. Vishwanath, and O. I. Motrunich, The half-filled Landau level: The case for Dirac composite fermions, *Science* **352**, 197 (2016).

[68] B. A. Bernevig and F. D. M. Haldane, Model fractional quantum Hall states and Jack polynomials, *Phys. Rev. Lett.* **100**, 246802 (2008).

[69] A. Sterdyniak, N. Regnault, and B. A. Bernevig, Extracting excitations from model state entanglement, *Phys. Rev. Lett.* **106**, 100405 (2011).

[70] A. P. Reddy, N. Paul, A. Abouelkomsan, and L. Fu, Non-Abelian fractionalization in topological minibands, *Phys. Rev. Lett.* **133**, 166503 (2024).

[71] Y.-L. Wu, N. Regnault, and B. A. Bernevig, Bloch model wave functions and pseudopotentials for all fractional Chern insulators, *Phys. Rev. Lett.* **110**, 106802 (2013).

[72] Y. Park and F. D. M. Haldane, Guiding-center hall viscosity and intrinsic dipole moment along edges of incompressible fractional quantum Hall fluids, *Phys. Rev. B* **90**, 045123 (2014).